

not influence the value of the incommensurate vector  $Q$  because the fluctuations are slow. The point is that the semiclassical analysis is based on relatively short distance and time, with corresponding typical momenta and energies  $Q < q_{\text{semi}} < p_F \propto \sqrt{x}$ ,  $\omega_{\text{semi}} \sim \epsilon_F \propto x$ . Quantum fluctuations come from smaller momentum/energy scales  $q_{\text{quant}} < Q$ ,  $\omega_{\text{quant}} \propto x^{3/2}$ , as discussed in Ref. 29.

In the double layer case, one has to include the interlayer hopping in the effective action (2). As a result, holon wave function  $\psi$  attains bonding/antibonding index with respect to the interlayer hybridization [30]. The holon energy at *each of the two nodal points* reads  $\epsilon(\mathbf{p}) = \beta \mathbf{p}^2/2 \pm gQ \pm \Delta/2$ , where  $\pm gQ$  is the pseudospin splitting and  $\pm \Delta/2$  is the antibonding(a)/bonding(b) splitting. Effectively there are *four* different bands per nodal direction ( $b-$ ,  $b+$ ,  $a-$ ,  $a+$ ), altogether *eight* bands. The filling configuration of these bands is determined by minimizing the semiclassical energy, which yields three different doping regimes [30]

$$\begin{aligned} 1) \quad & x < x_0, \quad Q = 0 \\ 2) \quad & x_0 < x < x_1, \quad Q = \frac{g}{\rho_s} \frac{x - \Delta/(\pi\beta)}{3 - 2\lambda} \\ 3) \quad & x > x_1, \quad Q = gx/\rho_s, \end{aligned} \quad (3)$$

where  $\lambda = 2g^2/(\pi\beta\rho_s)$ . The points  $x_0$  and  $x_1$  are Lifshitz points. Filling configuration of these three regimes are shown in Fig.1. Areas of the filled holon pockets are

$$\begin{aligned} 1) \quad & A_{b-}/A_{\text{BZ}} = A_{b+}/A_{\text{BZ}} = x/2 \\ 2) \quad & A_{b-}/A_{\text{BZ}} = x/3 + gQ/(3\pi\beta) + \Delta/(6\pi\beta) \\ & A_{b+}/A_{\text{BZ}} = x/3 - 2gQ/(3\pi\beta) + \Delta/(6\pi\beta) \\ & A_{a-}/A_{\text{BZ}} = x/3 + gQ/(3\pi\beta) - \Delta/(3\pi\beta) \\ 3) \quad & A_{b-}/A_{\text{BZ}} = x/2 + \Delta/(4\pi\beta) \\ & A_{a-}/A_{\text{BZ}} = x/2 - \Delta/(4\pi\beta). \end{aligned} \quad (4)$$

Note that the total occupied area is  $2x$  because there are two layers. From (4) we conclude that there is one MQO frequency in the first regime, three frequencies in the second regime, and two frequencies in the third regime. Let us consider two scenarios for the doping dependence of the hybridization splitting: (A) a constant gap  $\Delta = \Delta_0$ , (B)  $\Delta = \Delta_0(1 + \nu x)$ , since the splitting  $\Delta$  is due to tunneling via interlayer oxygen chains [31], a linear dependence on doping is possible.

Values of the incommensurate wave vector  $Q$  determined by neutron scattering [19–21] are presented in Fig.2. Comparing Fig.2 with Eqs.(3) one finds  $x_0 \approx 0.06$ ,  $x_1 \approx 0.13$ . Using Eqs.(3), we can determine parameters of the model. We fix  $g = J$  and  $\rho_s = 0.175J$ , as they are predicted by the extended  $t$ - $J$  model. Within the scenario (A) the fit gives,  $\lambda = 1.23$ ,  $\beta = 2.95J$  ( $m^* = 1.35m_e$ ),  $\Delta_0 = 0.556J$ . Within the scenario (B), the data from Fig.2 are not sufficient to determine the additional parameter  $\nu$ . However, we can assume that value of  $\lambda$  in

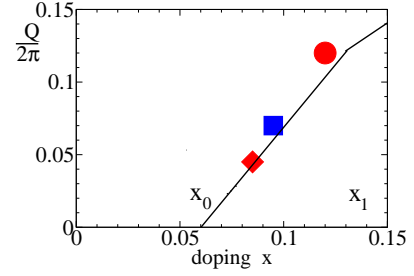


FIG. 2: (color online) Incommensurate wave vector versus doping. The blue square [19], the red circle [20], and the red diamond [21] show neutron scattering data. The solid line shows fit of the data using Eqs.(3).

YBCO and LSCO is the same, and use the value  $\lambda = 1.31$  obtained in Ref. [29] from fitting the data for LSCO. This gives  $\beta = 2.78J$  ( $m^* = 1.43m_e$ ),  $\Delta_0 = 0.37J$ ,  $\nu = 6.9$  within the scenario (B). Note that values of  $\beta$  in both fits are close to that predicted by the extended  $t$ - $J$  model, as demonstrated in the paragraph after Eq.(2), and the corresponding effective masses are close to that measured in MQO away from the QCP [11, 12],  $m^* = 1.6 \pm 0.1m_e$ .

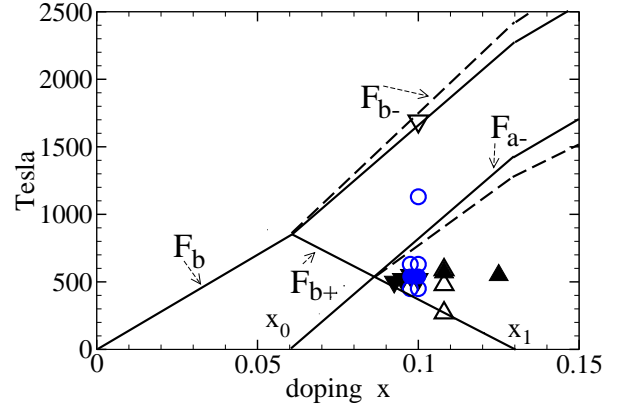


FIG. 3: (color online) Frequencies of MQO in Tesla versus doping. Solid lines show the theoretical prediction within the scenario (A), dashed lines show the prediction within the scenario (B). Predictions (A) and (B) coincide in the lower part of the figure. Experimental data are shown by symbols: Ref. [9] - blue circles, Ref. [11] - black triangles down, Ref. [12] - black triangles up. Full symbols correspond to maximum intensity lines.

Frequencies of MQO are determined by these parameters via Eqs.(4) and (1). The results are presented in Fig.3. Difference between the scenario (A) (solid lines) and the scenario (B) (dashed lines) is fairly small. There is quite a reasonable agreement with experimental data, especially having in mind that the theory has no fitting parameters related to MQO. Even a high frequency point  $\approx 1690T$  is reproduced. Notice that MQO always contain higher harmonics. Most likely the blue circle at  $\approx 1100T$  is such a harmonic [11]. Filling of each pocket is only a fraction of the total doping, this explains why the filling extracted from one single frequency seems to violate the Luttinger sum rule. The main frequency at  $x \approx 0.09$  comes from the  $b+$  pocket, which has Fermi